Roman Coronagraph Instrument Post Processing Report - OS9 HLC Distribution

April 3, 2021

Marie Ygouf[1], Neil Zimmerman[2], Vanessa Bailey[1], John Krist[1], Rob Zellem[1], John Debes[3]

1. Jet Propulsion Laboratory, California Institute of Technology
2. Goddard Flight Space Center
3. Space Telescope Science Institute

Contents

[1]This paragraph was written using information from John Krist's OS9 slide package on the IPAC website and Bijan Nemati CGI Detector Simulator communication on Feb 11 2020. Please see Nemati (2020) for more information about the photon counting mode of Roman CGI.

1 Introduction

This document reports on findings from applying post-processing techniques to the Observation Scenario 9 - Hybrid Lyot Coronagraph simulated data for the Roman Space Telescope Coronagraph Instrument. This is an on-going work and thus the information contained in this document is subject to future updates. In the meantime, please send questions and/or comments to marie.ygouf@jpl.nasa.gov.

1.1 Key Definitions

ADI: Angular Differential Imaging
CGI: Coronagraphic Instrument
DM: Deformable Mirror
EFC: Electric Field Conjugaison
EMCCD: Electron Multiplying Charge Coupled Device
FAC: Factor Above Classical (also called "post-processing factor (fpp)" in some documents)
FPM: Focal Plane Mask
HLC: Hybrid Lyot Coronagraph
JPL: Jet Propulsion Laboratory
LOWFS/C: Low Order Wavefront Sensing and Control
MUFs: Model Uncertainty Factors
OS: Observing Scenario
PCA: Principal Component Analysis
PSF: Point Spread Function
QE: Quantum efficiency
RDI: Reference Star Differential Imaging
STOP: Structural Thermal Optical Performance
WFI: Wide Field Instrument

2 Data Description

2.1 OS9 Simulation

The Observing Scenario (OS) image time sequences are generated by John Krist and the integrated modeling team at JPL to create simulated CGI data for the Hybrid Lyot Coronagraphc (HLC) which includes the most updated concept of operations observing strategy. For this work, we used the most recent OS dataset made public on May 6th 2020, called OS9 [2], with the broadband HLC-20190210 (Phase B flight design) in a 10% bandpass filter centered at 575 nm (Band 1: 546 - 603 nm). The target star used for these simulations is 47 UMa (V=5.0 mag, G1V) and the reference star is ζ Pup (V=2.25 mag, O4I). This is the first time this star is used as a reference in one of the Roman observing scenarios. Although being located 90 degrees away from 47 UMa, this new reference star was selected because

[2] https://roman.ipac.caltech.edu/sims/Coronagraph_public_images.html#CGI_OS9

it is only 3.5 degrees different in solar pitch from 47 UMa (see paragraph 2.2.2 for more information). The stellar spectra of the two stars (G1V and O4I), and stellar diameter are included. Two planets of contrast 1×10^{-8} and 3×10^{-9} were injected at separations of $3.5\lambda/D$ and $4.5\lambda/D$ respectively.

The observing sequence begins with a slew from a Wide Field Instrument (WFI) high latitude survey target to the reference star, followed by an observatory settling time of 30 hours. Assuming that the dark hole was previously dug at some earlier time, the observation cycle starts with 4 hours of dark hole touchup or Electric Field Conjugaison (EFC) maintenance on ζ Pup. One EFC iteration is performed every 2 hours for a total of 2 iterations over each 4 hour touch-up span. Then, one hour is spent on the imaging of ζ Pup before slewing to the target star 47 UMa. The target is observed for about 1.5 hours at rolls angles of -11°, +11°, -11°, +11° relative to the solar-normal roll before slewing back to ζ Pup for about one hour of imaging. This observation cycle is repeated 3 times for a total of 18 different target pointings. Figure 1 shows a visualization of the observing time series is presented in OS9. Note that the data corresponding to the EFC maintenance at the beginning of each cycle is not included in the OS9 distribution.

The STOP model was run with 20 min timesteps to produce aberration timeseries and results were interpolated to 5 min timesteps. The STOP model assumed instantaneous slews, but the jitter model included slew/roll times. Slew times were taken out of STOP on-target times, resulting in an irregular number of timesteps on each star/roll. These issues will be fixed in future scenarios. Speckle images were interpolated in time to produce images at EMCCD framerates (5 s for target, 60 s for reference), binned to the detector resolution (0.021 arcsec = $0.42\,\lambda_c/D$), and fed into the EMCCD model in the case of noisy data. The OS9 distribution includes: 335 reference images at 60 seconds each for a total of 5.58 hours, 7080 target star images at 5 seconds each at -11° roll and 7320 target star images at 5 seconds each at +11° roll, for a total of 20 hours. The exposure times per frame for both stars depend on their brightness and whether they are observed in "analog" or "photon-counting" mode (see section 3.1 for more details). Table 1 summarizes the modeling timesteps.

These simulations include wavefront error changes from thermal drift, errors from Low Order Wavefront Sensing and Control (LOWFS/C) (Z4 – Z11 LOWFS sensed & corrected with measurement & DM errors), errors from beam shears, DM thermal drift (from mini-STOP CGI-only model) and pointing jitter (LOWFS-corrected), all optical aberrations, including polarization, Focal Plane Mask (FPM) fabrication errors and EMCCD noise. Sources of noise included in the EMCCD noise model are shot noise, dark current and read noise. No cosmic rays, traps or hot pixels are included in this dataset.

These simulations were repeated to produce eight different datasets: noiseless and noisy, with and without optical model uncertainty factors (MUFs), with and without injected planets (see Table 2). Only noisy data are fed into the EMCCD model. Thus, noiseless data are given in flux units while noisy data are in CCD data numbers. Of the previous versions of OS data, only OS6 did include MUFs. The optical MUFs are: Polarization aberrations = 1.5×, contrast sensitivity to low-order aberrations = 2.0× (includes sensitivity to polarization and wavefront jitter), starting contrast = 2.0×, structural deformation = 2.0× (includes beam shear increases and wavefront error drift), and frequency dependent jitter = 3.0× (<20 Hz), 4.27× (40-100 Hz) and 8.0× (>100 Hz) (in Phase A, OS6: 2.07× (<20 Hz), 4.27× (>40 Hz)).

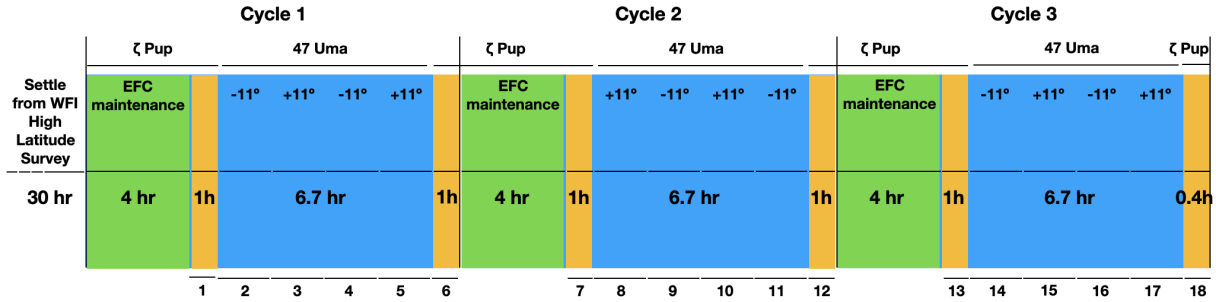

Figure 1: Visualization of the observing sequence simulated in the OS9 HLC PSF time series. The sequence begins with a slew from a WFI high latitude survey followed by an observatory settling time of 30 hours. Then Cycle 1 begins with 4 hours of EFC maintenance on the reference ζ Pup (green), about 1 hour observing ζ Pup (yellow) and about 6.67 hours observing the target 47 UMa (blue) at two different roll angles before going back to the reference for an additional hour (yellow). This cycle is repeated 3 times in total with a slightly less observing time for ζ Pup at the end of the third cycle. Data corresponding to the EFC maintenance are not included in the OS9 distribution.

Cycle #	Target pointing #	Target	Roll angle (°)	Exp. time/frame (sec)	# of frames	Total Exp. Time (sec)
1	1	ζ Pup	-11	60	60	3600
	2	47 UMa	-11	5	1020	5100
	3	47 UMa	+11	5	1260	6300
	4	47 UMa	-11	5	1260	6300
	5	47 UMa	+11	5	1260	6300
	6	ζ Pup	+11	60	65	3900
2	7	ζ Pup	+11	60	60	3600
	8	47 UMa	+11	5	1020	5100
	9	47 UMa	-11	5	1260	6300
	10	47 UMa	+11	5	1260	6300
	11	47 UMa	-11	5	1260	6300
	12	ζ Pup	-11	60	65	3900
3	13	ζ Pup	-11	60	60	3600
	14	47 UMa	-11	5	1020	5100
	15	47 UMa	+11	5	1260	6300
	16	47 UMa	-11	5	1260	6300
	17	47 UMa	+11	5	1260	6300
	18	ζ Pup	+11	60	25	1500
				Total	14735	92100

Table 1: Modeling Timesteps for target 47 UMa and reference ζ Pup. The entire observing sequence is 25.58 hours long (excluding the EFC maintenance) and 37.58 hours long (including the EFC maintenance, not described in this table). Data corresponding to the EFC maintenance are not included in the OS9 distribution.

File name	MUFs	Noise	Planets	Flux Units
os9_noiseless_ccd_images_no_planets.fits	-	-	-	average flux units
os9_noiseless_ccd_images_with_planets.fits	-	-	✓	average flux units
os9_ccd_images_no_planets.fits	-	✓	-	EMCCD counts
os9_ccd_images_with_planets.fits	-	✓	✓	EMCCD counts
muf_os9_noiseless_ccd_images_no_planets.fits	✓	-	-	average flux units
muf_os9_noiseless_ccd_images_with_planets.fits	✓	-	✓	average flux units
muf_os9_ccd_images_no_planets.fits	✓	✓	-	EMCCD counts
muf_os9_ccd_images_with_planets.fits	✓	✓	✓	EMCCD counts

Table 2: Description of OS9 HLC Datasets.

2.2 Differences with previous observing scenarios

The successive observing scenarios that have been simulated since OS1 take into account the evolution of telescope and instrument design as well as the most updated concept of operations observing strategy. This section covers the major differences between the OS9 and the OS6[3], for which a similar data processing and analysis was performed (Zimmerman et al., 2018).

2.2.1 Observing strategy

Both observing scenarios follow the same pattern of two pairs of science target observations at each roll angle. One difference rests in the way a cycle is defined. For OS6, a cycle is defined by one reference star observation followed by two repetitions of a pair of two roll angle observations of the science target. For OS9, this is the same pattern but with an additional observation of the reference star at the end of the cycle.

The number of cycles is smaller for OS9 HLC (3 cycles, which is representative of an HLC direct imaging set) compared to OS6 (13 cycles, designed for total lengths representing shaped pupil coronagraph spectral observations). OS9 HLC totals about 26 hours of observing time including about 20 hours on the target 47 UMa and about 6 hours on the reference ζ Pup, which is a more realistic duration for observations with the Hybrid Lyot Coronagraph. In comparison OS6 totals about 120 hours of observing time including about 95 hours on 47 UMa and about 24 hours on ζ Pup.

Another difference between OS9 and OS6 is the 4-hour Electric Field Conjugation (EFC) maintenance on ζ Pup (1 iteration every 2 hours) that is performed at the beginning of each cycle in OS9. Those EFC data are not included in the distribution.

Finally, the roll angles were reduced from +13/-13° in OS6 to +11/-11° in OS9 because of the change in reference star. The roll limits are set by:

- which objects we are looking at in time and with respect to solar attitudes;
- the length of the observation;

[3]Note that no end-to-end simulations were performed for OS7 and OS8.

- whether a constant position angle constraint (position of the camera axes projected on-sky fixed) is imposed, which is the case for observing scenario OS6 and beyond including OS9.

Unlike the Hubble Space Telescope that allows a wider range for authorized roll angles, the solar panels in Roman are fixed and so pointings are more restricted. Note that a larger delta roll is possible for shorter observations and/or if the constant position angle constraint isn't imposed.

2.2.2 Astrophysical targets

The target, 47 UMa has been used for all observing scenarios since OS1. This is the first time ζ Pup is used as a reference star. In the previous observing scenarios, β UMa and η UMa were both used. A higher-fidelity observatory model incorporated in OS8 simulations showed a greater sensitivity of the primary mirror wavefront to the solar pitch angle. This motivated switching the reference star to ζ Pup for OS9 for which the difference in solar pitch angle with 47 UMa is smaller (3.5 degrees instead of $\sim$ 15 degrees for previous reference stars). This reduced aberration drifts by over an order of magnitude. Most importantly, it reduced high-order spherical aberration drifts, which LOWFS cannot sense or control, to negligible levels.

2.2.3 Telescope and Instrument Modeling

The STOP model consists of nodes forming the mesh that represents the structure of the telescope and CGI (the wireframe representation of the system). A more realistic STOP model with more nodes was used in OS9. Also, the observatory model changed significantly between OS6 and OS9 (completely different forward sunshield).

A detector model was applied to the Roman CGI images distributed with the public release. This detector model converts the noiseless speckle images to noisy images that would be obtained on the CGI EMCCD. In particular, speckle images were interpolated in time to produce images at EMCCD framerates (5s for target, 100s for reference), binned to the detector resolution (0.021 arcsec = 0.42 λ_c/D), and fed into the EMCCD model. It is assumed that the reference star is bright enough to be observed in "analog" mode while the target star is observed in "photon-counting" mode (see Section 3.1 for more details about the observing modes). It is worth noting that a slightly different detector model was applied when processing the OS6 data (Zimmerman et al.). That model did not correctly adjust for coincidence and threshold losses like the more realistic model applied to OS9 data (Section 3).

Compared to OS6, more errors are included in the OS9 distribution, such as a more realistic DM behavior and more realistic treatment of the telescope primary mirror deformations.

3 Data Reduction Procedure

3.1 Roman CGI EMCCD and Photon Counting Mode[4]

3.1.1 Analog and Photon Counting mode in EMCCDs

The Roman Space Telescope CGI will use an Electron-Multiplying CCD (EMCCD) as a detector. Similarly to CCDs', EMCCDs' counts are electrons generated by photons, detector noise (shot, dark, etc...) and read noise amplified by a gain. EMCCDs are different from CCDs in the way they use a high voltage gain register in place of a traditional serial register. The high voltage gain register amplifies the signal before read noise is added, which reduces read noise in proportion. Roman CGI's EMCCD will be used in two operation modes: low gain (<1000) or "analog mode" and high gain (>1000) or "photon counting" mode. The analog mode, which is similar to how regular CCDs are operated, will be used to observe the reference star. On the other hand, the target star will be observed in photon counting mode.

3.1.2 The need for Photon Counting mode in Roman CGI

Because of the very low signal we are trying to detect when observing the target star (photon rate of 3 milliphotons/pix/sec for a 26-magnitude planet) combined to a very low telescope throughput for an off-axis object (1.6%), a high integration time is needed. On the other hand, in space, cosmic rays limit single-frame integration times to a few hundred seconds. Under these conditions read noise is dominant (100 e- RMS per frame) over the electrons generated by the photons and other detector noises (shot, dark, etc). This would lead to unpractical levels of read noise if a traditional CCD was to be used. Instead, the Roman Space Telescope EMCCD uses signal amplification from a gain register prior to read out to effectively remove read noise. This reduction comes at the cost of an increase (by a factor of $\sim \sqrt{2}$), called as Excess Noise Factor (ENF) of all other noises. This latter disadvantage can be mitigated using a processing technique called photon counting.

3.1.3 Photon Counting Principles

In photon counting, a high gain (1000 or more) is applied to each EMCCD frame. A threshold factor, typically a few times (5 is usually good) the read noise, is chosen. Any pixels with counts below the threshold are recorded as zero electrons, while any above are recorded as one electron. No more than 1 electron will ever be recorded, regardless of how many input electrons generated the signal. It is therefore critical, when operating in this mode, to select a frame time such that the brightest pixel in the image has a mean count rate of <0.1 photons/frame. The final image is the sum of separate photon-counted frames. Photon counting incurs two losses that must be corrected:

[4]This paragraph was written using information from John Krist's OS9 slide package on the IPAC website and Bijan Nemati CGI Detector Simulator communication on Feb 11 2020. Please see Nemati (2020) for more information about the photon counting mode of Roman CGI.

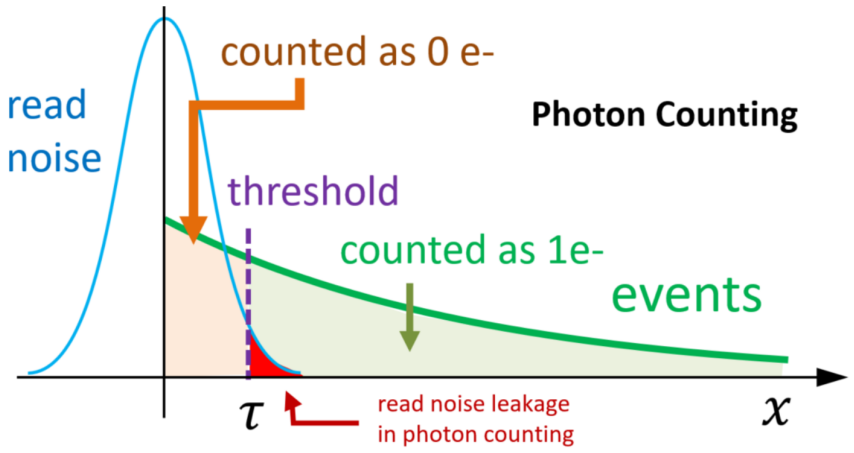

Figure 2: Photon Counting rejects read noise and eliminates ENF at the expense of some efficiency loss. Any pixels with counts below the threshold are recorded as zero electrons, while any above are recorded as one electron. Figure from Nemati et al. 2020.

- *Threshold loss.* Applying a threshold means some real events are lost. In that case, a real photo-electron event is rejected because it failed the threshold cut. This effect is called the threshold loss. The thresholding efficiency is defined by: $\epsilon_{PC} = e^{-\frac{n\sigma}{g}}$, where n is the threshold factor σ the read noise and g the gain.

- *Coincidence loss.* In addition, the stochastic photon arrival times mean that occasionally more than one photon will arrive in the same pixel in a given frame. This event would still be counted as a single electron, and this signal undercount is referred to as "coincidence loss." The coincidence loss is defined by: $\epsilon_{CL} = \frac{1-e^{-\lambda}}{\lambda}$, where λ is the real photons/pixel/frame.

The measured mean count rate per frame corrected from those losses is $\lambda\epsilon_{PC}\epsilon_{CL}$. λ is solved for each pixel: $\lambda = -\ln(1 - \frac{\lambda_{tot}}{e^{-\frac{n\sigma}{g}}}(\frac{t_f}{t_{tot}}))$, where λ_{tot} is the total measured photon/pix/sec rate, t_{tot} is the total exposure time and t_f is the single frame time. This solution excludes quantum efficiency (QE), which is not simulated in OS9. In addition, leakage from detector effects also occurs. This leakage, not simulated in OS9, can be mitigated as described in Nemati (2020).

It is planned to apply this photon-counting strategy to each EMCCD frame taken at high gain (> 1000), which will be the case for the target star. The reference star, which should be brighter than the target star may be treated differently. Due to coincidence issues, bright stars have fluxes too high for photon counting (too many counts per shortest possible exposure) and so must be imaged in "analog mode". In this mode, a smaller gain will be applied without the need for photon-counting processing. For those data the incident flux is obtained by dividing the counts by the gain, just like in a traditional CCD. Table 3 summarizes the EMCCD setup for the target and reference stars.

Star	Exp. time/fr. (s)	Detector Mode	EM gain
47 UMa	5	Photon-counting	6000
ζ Pup	60	Analog	100

Table 3: EMCCD setup for target and reference stars.

3.2 Pre-processing

Before applying post-processing to the OS9 data, several pre-processing steps are needed:

- Step 1: Data extraction;
- Step 2: Photon-counting procedure for "photon-counting" mode data or gain correction for analog mode data. ;
- Step 3: Normalization to the flux incident on the illuminated area of the primary mirror.

It is worth noting that no cosmic rays or traps are including in the OS9 data sets. There is no need for procedures to correct those effects. Similarly, there is no need for dark subtraction or flat fielding. However, those effects will need to be corrected during the Roman CGI operations.

3.2.1 Step 1: Data extraction

We extracted data frames from all pointings from each observation cycle for the reference star, and for the target at rolls +11° and -11° for each of the four available datasets. We obtained 3 data cubes, one for the reference, and one for the target at each roll. Table 4 summarizes the dimensions for each of those tables. It is worth noting that the total number of frames is different for each pointing. Also, even though the number of pixel per frame is different for noiseless (47×47) and noisy data (67×67), they both have a sampling of $0.42\lambda_c/D$ corresponding to the EMCCD resolution. The noisy data were zero-padded and thus have a bigger number of pixels than noiseless data. Figure 3 shows the first frames of those data cubes for the noisy case without model uncertainty factor.

3.2.2 Step 2: Photon counting and analog gain correction (noisy data only)

The target is observed in "photon counting" mode, which means that a photon counting procedure involving a thresholding and a correction factor for thresholding and coincidence losses must be performed on each target frame before coadding the frames and obtain the pre-processed data (see section 3.1 for more details about the photon-counting mode). Recall that OS9 noiseless data are in average flux units, and they do not have photon quantization or an EMCCD model applied. Therefore, there is no need to apply the photon-counting processing to noiseless data. The following steps were performed for each pointing of each noisy target data cube at both -11° and +11°:

Target	Target pointing #	Cube dimensions
ζ Pup	1	npix × npix × 60
	6	npix × npix × 65
	7	npix × npix × 60
	12	npix × npix × 65
	13	npix × npix × 60
	18	npix × npix × 25
47 UMa -11°	2	npix × npix × 1020
	4	npix × npix × 1260
	9	npix × npix × 1260
	11	npix × npix × 1260
	14	npix × npix × 1020
	16	npix × npix × 1260
47 UMa +11°	3	npix × npix × 1260
	5	npix × npix × 1260
	8	npix × npix × 1020
	10	npix × npix × 1260
	15	npix × npix × 1260
	17	npix × npix × 1260

Table 4: Cubes dimensions for each pointing, with npix equal to 47 and 67 for noiseless data and noisy data respectively.

- Apply threshold to each frame of data cube. We chose a threshold factor of 5 (5 times read noise, note that read noise can be found in the FITS header) in this case. Binary images were obtained in output;
- Co-add frames in data cube along the temporal dimension;
- Correct for the coincidence and threshold losses;
- Background correction is performed by averaging a subset of 36 pixels in the corner of the image;
- Normalization by the frame exposure time to obtain an image in count/sec.

After this processing, each data cube of dimension (6 × npix × npix, npix=47 for noiseless data and npix=67 for noisy data) is composed of 6 averaged frames, one per pointing. Figure 5 shows the coadded frames after applying the photon counting processing for the noisy case without MUF.

Data cubes for the reference star, as well as all noiseless data cubes do not need to be photon-counted. However, two steps need to be performed to preprocess those data cubes:

- Co-add frames in data cube along the temporal dimension;
- Normalization by the frame exposure time to obtain an image in count/sec;
- Dividing by the gain in the case of noisy data for reference the star (note that the gain can be found in the FITS header).

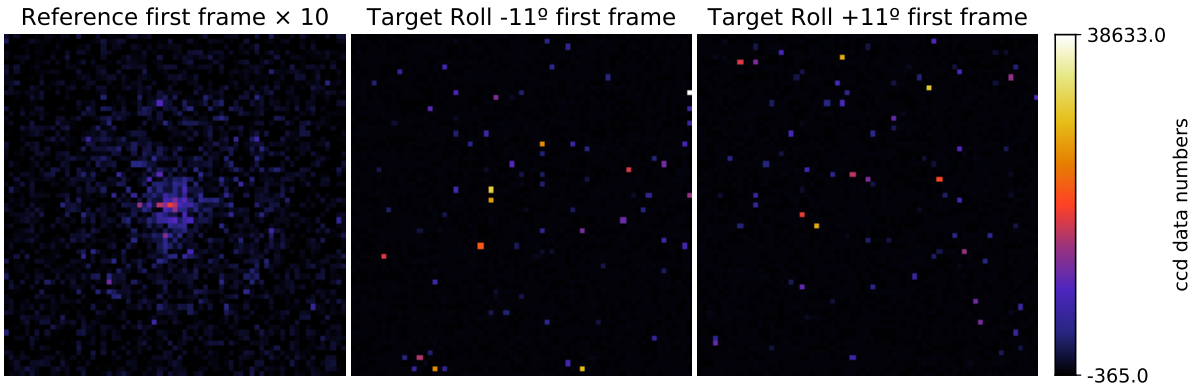

Figure 3: Raw EMCCD frames in analog (reference) and photon-counting (target) mode for the noisy case with planets and with MUFs. Note that the reference frame is multiplied by 10 for visualization.

3.2.3 Step 3: Normalization

At the end of step 2, the data units are count/sec. In step 3, we normalize the data to contrast units. In order to perform this step, we need to estimate the peak flux of the unocculted point spread function (PSF) at the detector sampling.

The OS9 distribution contains images of a flat-spectrum source offset by various amounts in radius and angle from the center of the FPM over one quadrant of the dark hole. It is a [nx,ny,r,θ] = [200,200,19,10] array. Those images are normalized to the flux incident on the illuminated area of the primary mirror (primary-flux-normalized). There are no losses from reflections, filters, QE, etc, but losses from CGI's masks are included in the simulation. In the absence of masks, the total image intensity would be 1.0. These 200 x 200 pixel images are sampled by 0.1 λ_c/D.

We first need to resample source offset images to the detector pixel size (0.42 λ_c/D). Then we extract the maximum value from the entire datacube (5.5×10^{-3} and 9.6×10^{-3} for the noiseless and noisy data respectively). We divide the pre-processed target and reference star datacubes by this value to obtain primary-flux-normalized data cubes. Finally, we divide those cubes by the flux of star to obtain the normalization in contrast units.

The results of this preprocessing for the 4 different available datasets of the OS9 distribution (with or without noise and with and without MUFs) are shown in Figure 6.

3.3 Post-processing

3.3.1 Procedure

We applied different techniques of post-processing, taking advantage of both the Reference Star Differential Imaging (RDI) and Angular Differential Imaging (ADI) strategies. RDI consists in observing a reference star to calibrate the stellar residuals. ADI consists in calibrating the stellar residuals by observing the target at different rolls angles (e.g., +/- 11 degrees).

Two families of techniques were explored:

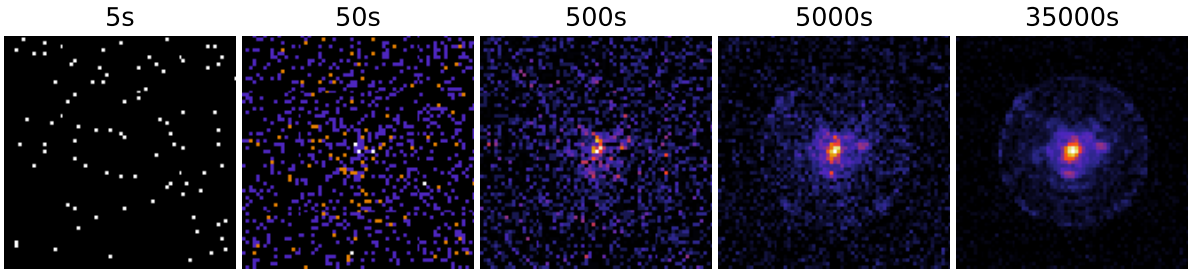

Figure 4: Illustration of photon-counting mode for the noisy case with planets and with MUFs. Photon counted data when increasing the exposure time from 5s (1 frame) to 35000s (7000 frames). All images are normalized to their maximum value and thus not on the same color scale.

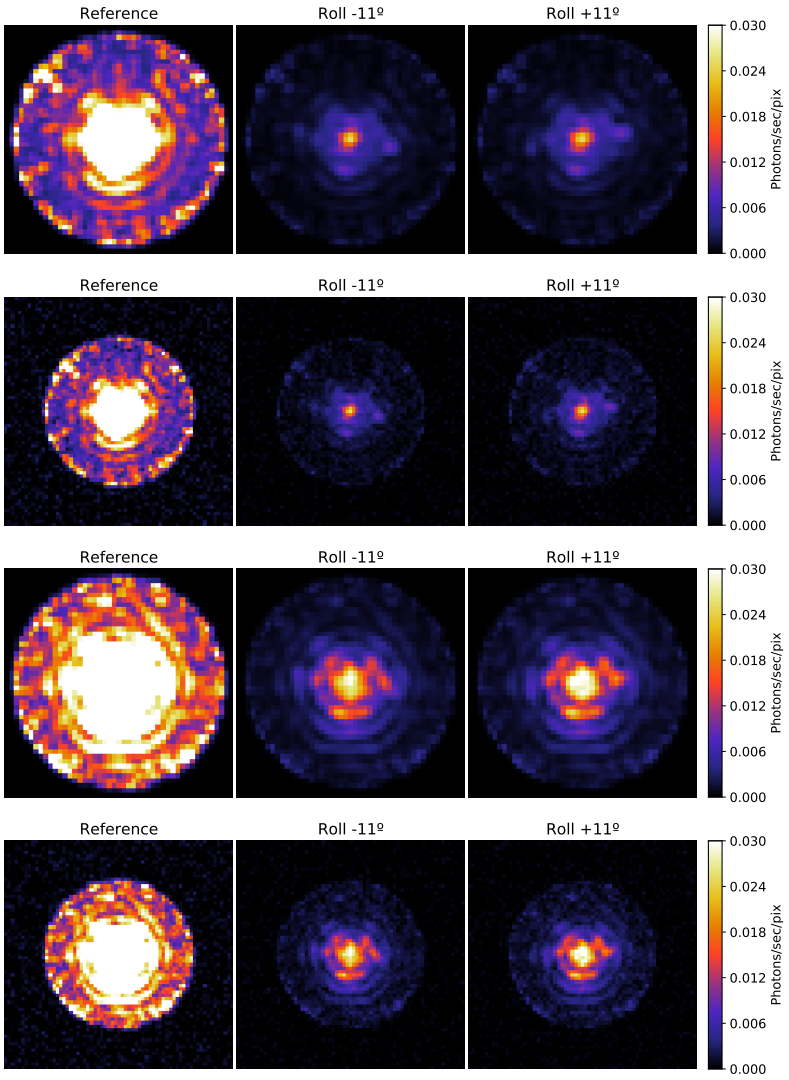

Figure 5: Gain corrected (reference) and photon-counted (target) data represented on the same color scale. From top to bottom: No MUF, Noiseless; No MUF, Noisy; MUF, Noiseless; MUF, Noisy.

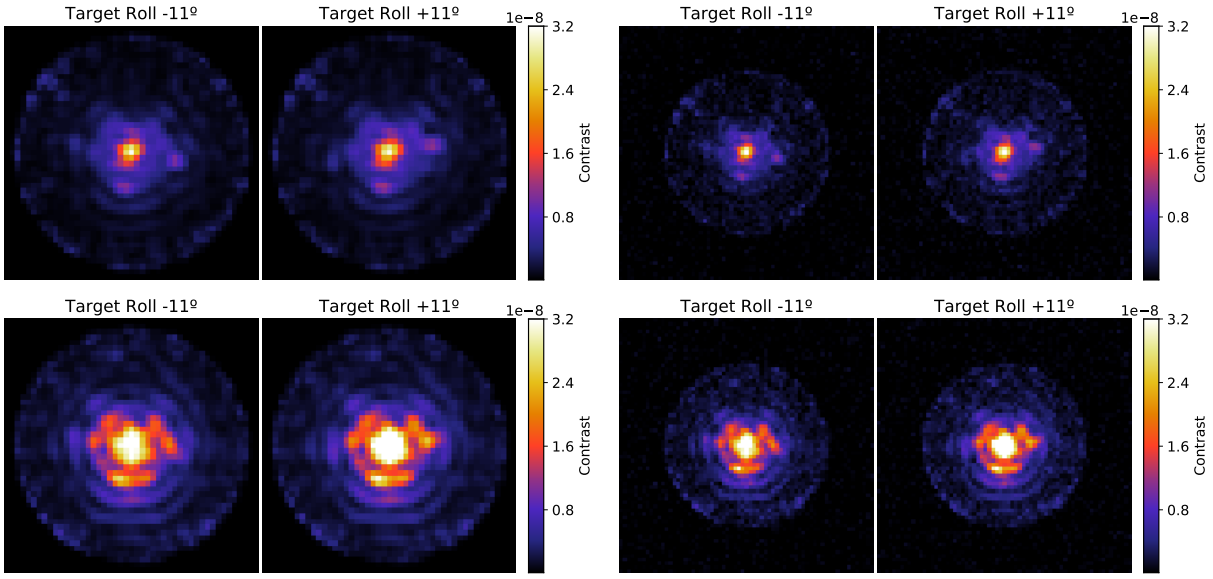

Figure 6: Pre-processed, coadded data for all datasets with planets in contrast units. [Top Left] No MUF, Noiseless. [Top Right] No MUF, Noisy. [Bottom Left] MUF, Noiseless, [Bottom Right] MUF, Noisy. Note that the resolution of those images is the same in the noiseless and noisy cases but the images appear smaller in the noisy case because they are zero-padded in the OS9 distribution.

- *Classical PSF subtraction.* Two flavors of this technique were implemented using either RDI or ADI, called cRDI and cADI respectively. Our implementation of classical PSF uses linear regressions to minimize the least square error in the final image (Figures 7 & 8);
- *Principal Component Analysis (PCA).* We used KLIP (Soummer et al. 2012), a Principal Component Analysis (PCA) technique that uses the reference cube as a library of reference point spread functions (Figure 9).

For the target at both rolls, each of the 12 target pointings (6 visits, 2 rolls each) was processed separately and combined at the end of the processing. We applied an annular mask, only taking into account the pixels that are comprised between 2.2 and 6 λ/D for both the regression and principal component analysis. The reason for this choice is that this region is the one we are the most interested in (the separations of the injected planets are $3.5\lambda/D$ and $4.5\lambda/D$ respectively) and using data outside of this region for post-processing may negatively impact the gain in this region.

Then, for RDI, we derotated the processed roll at $+11^{\text{º}}$ and coadded with the processed roll at -11º. Figure 7 represents our data processing using RDI.

For ADI we did the same thing using the -11° roll as a reference for the +11° roll and using the +11° roll as reference for the -11° roll. We then derotated the processed +11° roll that we coadded with the processed -11° roll as we did before for RDI. Figure 8 represents our data processing using ADI.

We performed those processing for the 4 different data sets of the OS9 distribution: with

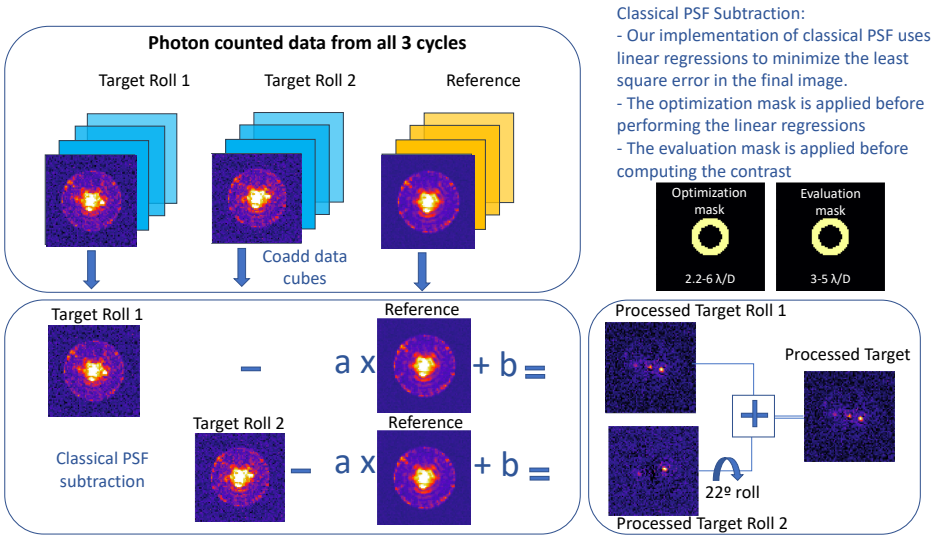

Figure 7: Performing Classical RDI (cRDI) PSF subtraction on OS9 HLC.

or without noise and with and without model uncertainty factor.

3.3.2 Results

Figure 10 shows the results of this processing for the processed cRDI, cADI and KLIP RDI data. Both planets at 1×10^{-8} and 3×10^{-9} are visible in the processed data for all 4 cases, being less visible in the noisy case where the noise is dominating over the speckles.

We computed contrasts and gains in the region we are the most interested in, which is between 3 and 5 λ/D. To calculate the contrast, we computed the standard deviation per pixel in the region of interest given by the annular mask for each of the 6 visits and we computed the median of those 6 visits. For KLIP reductions, we compensated for over-subtraction from algorithmic throughput using forward modeling. This technique consists in implementing the same processing applied on the images on sources offset by various amounts in radius from the center of the FPM, to estimate and correct for the impact of the post-processing algorithm on the planet throughput. Those computations were done on the data sets without planets to avoid any contamination from the planet signal. Note that the planets would need to be masked out if we were performing those computations on the data with planets.

The 5σ contrasts for the post-processed noiseless and noisy data are all below 2×10^{-9} and 9×10^{-9}, respectively, the noisy case with MUF being the worse case scenario. These values meet, with margin, the design requirement of 2.5×10^{-8} on the noisy data and the Threshold Technical Requirements 1×10^{-7}. In the noisy case, the noise is the limiting

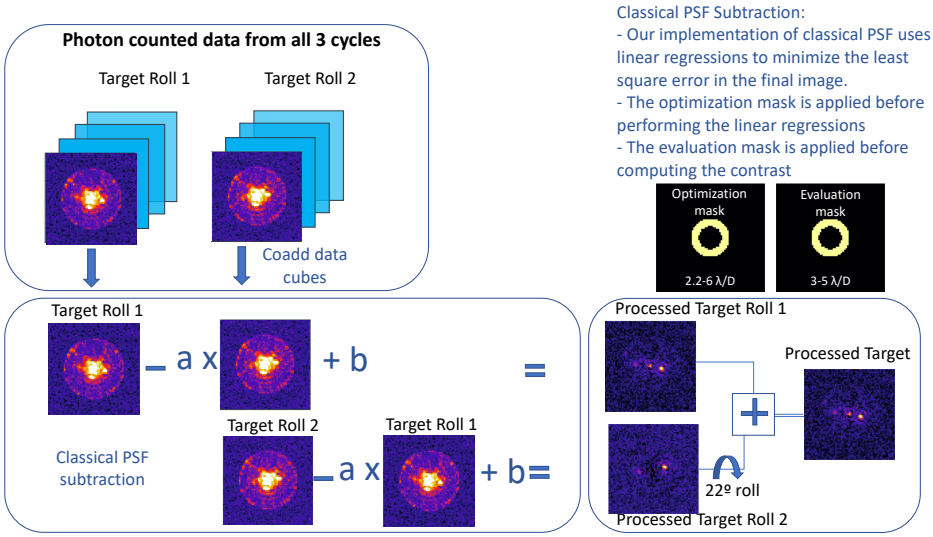

Figure 8: Performing Classical ADI (cADI) PSF subtraction on OS9 HLC.

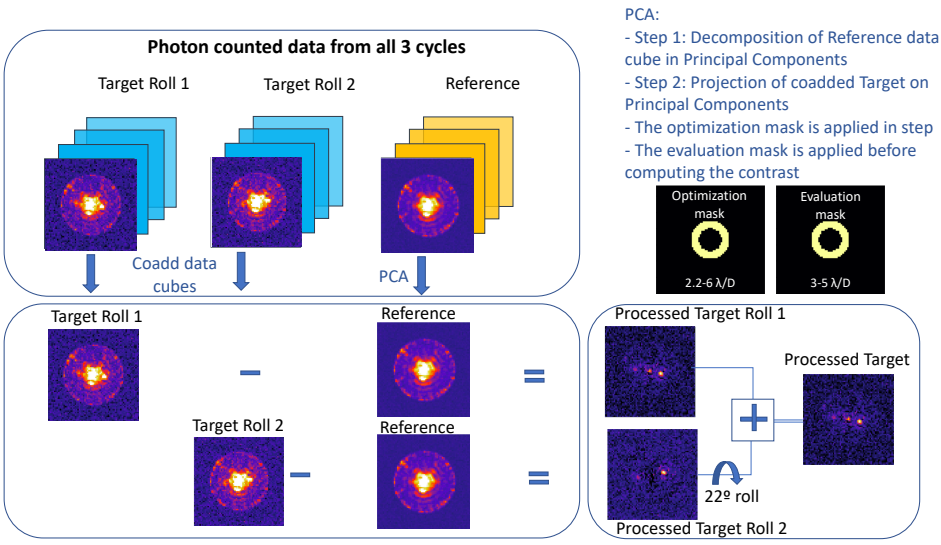

Figure 9: Performing KLIP RDI PSF subtraction on OS9 HLC.

factor, which explains the observed difference in sensitivities up to 1 magnitude.

The corresponding gains with respect to the unprocessed roll combined data vary quite a bit depending on if there is noise or not, the best gains (>6) being observed for the noiseless case. In the noisy case those gains decrease down to 1.8 for the noisy classical ADI. When comparing the performance of RDI vs ADI, the best gain is observed with ADI in the case of noiseless data. Indeed ADI usually provides more stable wavefront errors, which is important for classical PSF subtraction. On the other hand, RDI is performs better in the presence of noise. The higher shot noise from the science target speckles (versus the brighter reference star speckles) explains most of the difference in ADI performance as shown in Zimmerman et al.

We computed the Factor Above Classical (FAC), also called post-processing factor (fpp) in other documents, which is defined as the improvement in sensitivity over that achieved with classical RDI (or cRDI) PSF subtraction with a single observatory roll angle. This factor is defined for the noiseless case, because it is used in the CGI error budget as an assumed attenuation factor on the speckles only. The factor above classical is computed with respect to the single roll processed with classical subtraction. This factor is equal to 2.0 and 1.5 for the KLIP RDI roll combined processing without and with MUFs respectively, which is the expected order of magnitude for those scenarios. As a reference, we also computed the equivalent of those factors in the noisy cases without and with MUFs, which are equal to 1.7 and 1.2. This is well below 2 and this is due to the fact that we are noise dominated in this case and KLIP does not add much improvement with respect to the classical subtraction technique. Table 5 summarizes the sensitivities, gains and FAC for the 4 different data sets.

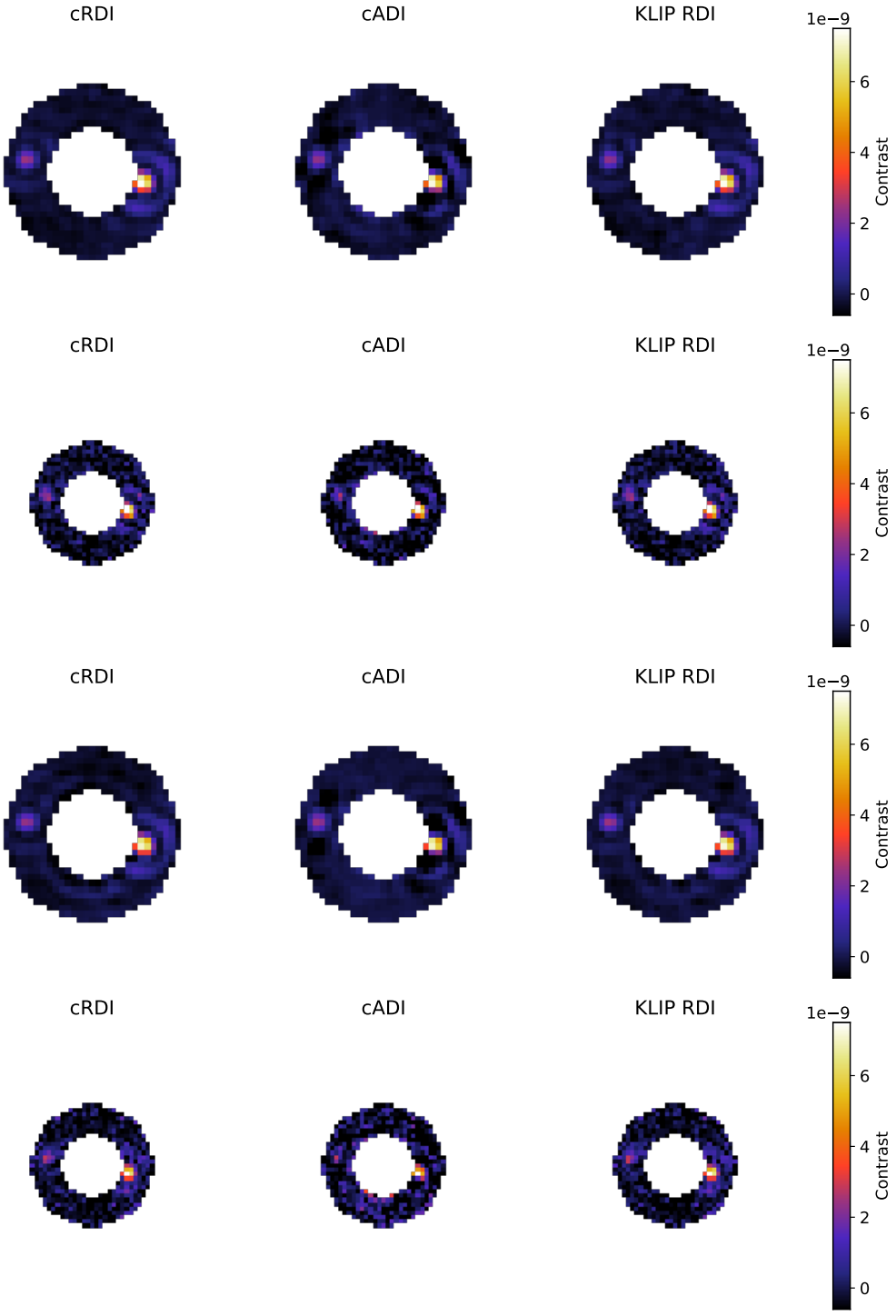

Figure 10: Datasets with planets processed with the 3 to $5\lambda/D$ annular mask with cRDI, cADI and KLIP ADI in contrast units. From top to bottom: No MUF, Noiseless; No MUF, Noisy; MUF, Noiseless; MUF, Noisy. Note that the resolution of those images is the same in the noiseless and noisy cases but the images appear smaller in the noisy case because they are zero-padded in the OS9 distribution.

	Noiseless			Noisy		
Post-Processing Method	5σ contrast	Gain	FAC	5σ contrast	Gain	FAC
No MUFs						
No sub., single roll minus	4.5×10^{-9}			8.3×10^{-9}		
No sub., single roll plus	4.8×10^{-9}			8.2×10^{-9}		
No sub., roll combined	4.1×10^{-9}			6.0×10^{-9}		
cRDI, single roll	7.2×10^{-10}	6.5		7.0×10^{-9}	1.2	
cRDI, roll combined	5.9×10^{-10}	6.7	1.0	4.5×10^{-9}	1.3	1.1
cADI, roll combined	4.0×10^{-10}	10.3	1.8	5.6×10^{-9}	1.02	0.9
KLIP RDI, roll combined	4.2×10^{-10}	10.9	1.7	4.7×10^{-9}	1.4	1.2
With MUFs						
No sub., single roll minus	1.5×10^{-8}			1.6×10^{-8}		
No sub., single roll plus	1.5×10^{-8}			1.8×10^{-8}		
No sub., roll combined	1.3×10^{-8}			1.4×10^{-8}		
cRDI, single roll	1.2×10^{-9}	12.9		8.4×10^{-9}	2.0	
cRDI, roll combined	1.1×10^{-9}	12.1	1.0	5.8×10^{-9}	2.6	1.3
cADI, roll combined	6.0×10^{-10}	22.3	1.9	7.5×10^{-9}	1.9	0.95
KLIP RDI, roll combined	6.1×10^{-10}	24.7	2.0	5.7×10^{-9}	2.9	1.5

Table 5: Summary of contrasts, gains and FAC for all four OS9 HLC datasets. Values are integrated over the annular mask for the region we are the most interested in, which is between 3 and 5 λ/D. The gain is defined by the ratio of contrast after post-processing to the roll combined raw contrast. The Factor Above Classical (FAC) is defined by the ratio of contrast after post-processing with cADI or KLIP to the single roll contrast.

4 Conclusion

We applied post-processing techniques to OS9 Hybrid Lyot Coronograph simulated data.

- The factor above classical is equal to 2.0 and 1.5 in the MUF/Noiseless and no MUF/Noiseless case scenarios respectively;
- The performance is better than the design requirement of 10σ flux ratio sensitivity of 5×10^{-8} for every case tested (with and without model uncertainty factor for both noiseless and noisy data);
- In the noisy case, photon noise, rather than residual speckles, is the limiting factor.
- The integrated contrast gain vs. raw contrast between 3 and 5 λ/D from classical PSF subtraction ranges from ~ 2 for the noisy case without model uncertainty factor to ~ 25 for the noiseless case with MUF factor;
- ADI performs better in the noiseless case, which is speckle dominated, and RDI performs better in the noisy case, which is shot noise dominated;
- The results, with MUFs applied, are all within a factor of 2 of the corresponding OS6 sensitivity and contrast gain factors. Despite the changes to the integrated model since 2018, including some new error sources and disturbances, the overall performance has not worsened dramatically.

5 Acknowledgment

The research was carried out at the Jet Propulsion Laboratory, California Institute of Technology, under a contract with the National Aeronautics and Space Administration (80NM0018D0004).

6 References

1. Nemati, "Photon Counting and Precision Photometry for the Roman Space Telescope Coronagraph", Proc. of SPIE, 2020.
2. Soummer et al., "Detection and Characterization of Exoplanets and Disks Using Projections on Karhunen-Loève Eigenimages", ApJ, 2012.
3. Zimmerman et al., "WFIRST Coronagraph Instrument post-processing algorithms for advanced PSF subtraction", 2018.
4. Ygouf et al., "Data processing and algorithm development for the WFIRST-AFTA coronagraph", Proc. of SPIE, 2016.

5. Ygouf et al., "Data Processing and Algorithm Development for the WFIRST-AFTA Coronagraph: Reduction of Noise Free Simulated Images, Analysis and Spectrum Extraction with Reference Star Differential Imaging", Proc. of SPIE, 2015.

6. Ygouf et al., "Data Post Processing and Algorithm Development for the WFIRST-AFTA Coronagraph", FY15 final report, Space Telescope Science Institute, 2016.

7. Ygouf et al., "AFTA Coronagraphic Technology – Data Post-Processing and Algorithm Development", FY14 final report, Space Telescope Science Institute, 2014.

8. Ygouf et al., "Data Post-Processing and Algorithm Development for the WFIRST-AFTA Coronagraph", First Progress Report, Space Telescope Science Institute, 2015.